Int. J. Electrochem. Sci., 17 **(2022)** Article Number: 221220, doi: 10.20964/2022.12.20

International Journal of
ELECTROCHEMICAL
SCIENCE
www.electrochemsci.org

Better Electrochemical Performance of PEMFC with a Symmetrical Serpentine Flow Field Bipolar Plate

Yanqiang Wei, Lifeng Xu, Yang Li, Jinzhu Tan[*]

School of Mechanical and Power Engineering, Nanjing Tech University, Nanjing, Jiangsu, 211816, China
[*]E-mail: tjznjut@njtech.edu.cn

Received: 19 August 2022 / *Accepted:* 23 October 2022 / *Published:* 17 November 2022

Proton exchange membrane fuel cell (PEMFC) has drawn widely attention as a promising power generation device. The structure design of flow field for bipolar plate is closely related to the output performance and service life of PEMFC. In this paper, a novel symmetrical serpentine flow field (SSFF) was proposed for improving mass transfer capability of the conventional serpentine flow field(CSFF). A single PEMFC with the SSFF bipolar plate was designed and studied. Two three-dimensional Computational Fluid Dynamics (CFD) models for the PEMFC with the CSFF bipolar plate and the SSFF bipolar plate were established based on CFD method. And then, numerical simulations were conducted using the FLUENT PEM fuel cell module. In addition, the electrochemical performance test was performed for the PEMFC with SSFF bipolar plate. The simulated results indicate that the PEMFC with SSFF bipolar plate had better oxygen transportation and better water removal than the PEMFC with CSFF bipolar plate. The results of both simulation and test show that the PEMFC with SSFF bipolar plate had better electrochemical performance than the PEMFC with CSFF bipolar plate. Specially, the maximum power density of the PEMFC was enhanced by 22.9% by adopting the SSCF bipolar plate.

Keywords: PEMFC; Bipolar plate; Symmetrical serpentine flow field; Numerical simulation; Electrochemical performance

1. INTRODUCTION

International energy shortage and environmental pollution have caused widespread concerns in the world, so it is imperative to find clean energy instead of traditional fossil fuels [1-2]. Fuel cells have attracted widely attention as a power generation device with less pollution to the environment [3-5]. Proton exchange membrane fuel cell (PEMFC) is considered as one of the most potential fuel cells due to its high electric efficiency, quick start-up, less pollution, low operating temperature and low noise [6-8]. A typical single PEMFC mainly includes proton exchange membrane (PEM), catalyst layers (CLs), gas diffusion layers (GDLs), gaskets, bipolar plate(BPP), current collectors，end plates and bolts [9-

10]. As a crucial component of PEMFC, bipolar plate accounts for 70% of total mass and about 30% of total cost [11-12]. The functions of bipolar plate include distributing the reactant gases, removing products and transporting electrons [13-14]. Therefore, performance of the PEMFC is closely associated with design of the flow field structure for bipolar plate.

Many scholars have studied different flow field structures how to influence the electrochemical performance of PEMFC. The researchers proposed a stepped flow field of bipolar plate for the PEMFC [15]. They found that the stepped flow field bipolar plate could improve distribution of reactants and removal of water. A trap-shape flow field bipolar plate for the PEMFC was studied [16]. The simulated results indicated that the flow field with two 8-mm-long traps provided considerably higher current densities, and improved the oxygen distribution and water removal. A novel pneumatic clamping mechanism was proposed for improving the electrochemical performance of PEMFC with the conventional three serpentine flow field bipolar plate in [17]. A leaf vein bionic flow field for the PEMFC was designed [18]. And the results showed that the PEMFC with the composite bionic flow field had good performance compared to the PEMFC with serpentine flow field, notably the maximum power density of the PEMFC was increased by 8.475%. The researchers analyzed conventional three serpentine flow field and parallel flow field with different depths based on experiment [19]. They found that the deep channel for flow field was beneficial to oxygen transportation and water removal. The PEMFC with the zigzag flow field bipolar plate was investigated in [20]. The results of simulation presented that the PEMFC with a zigzag flow field had lower transport resistance of reactants and higher transfer rates. A bionic flow field bipolar plate for the PEMFC was studied in [21]. The results of simulation presented that the PEMFC with the bionic flow field bipolar plate had better dynamic transmission characteristics and removal rate of droplet than the PEMFC with the serpentine flow field bipolar plate. The researchers investigated a PEMFC with the flow field with baffle plates [22]. They found that the flow field with 5 baffle plates for the PEMFC had the best electrochemical performance due to that the flow field with 5 baffle plates could significantly improve the reactant transportation and water removal.

Although there are many reports in the literature for different types flow field bipolar plate of PEMFC, few results were reported about the novel symmetrical serpentine flow field (SSFF) bipolar plate. In this paper, a new SSFF was presented. A single PEMFC with the new SSFF bipolar plate was designed and studied. And two three-dimensional CFD models for the PEMFC with the conventional serpentine flow field (CSFF) bipolar plate and the new SSFF bipolar plate were established based on Computational Fluid Dynamics (CFD) method. And then, numerical simulations were conducted using the FLUENT PEM fuel cell module. In addition, the electrochemical performance test was performed for the PEMFC with the new SSFF bipolar plate.

2. DESCRIPTION OF THE DESIGN

A new symmetrical serpentine flow field (SSFF) was presented in this paper and is shown in Fig. 1. The flow channels in Fig. 1 were marked in black, and the ridges in Fig. 1 were marked in white. Serial number 1 in Fig. 1 denotes the inlet of flow field, serial number 2 in Fig. 1denotes the outlet of flow field, serial number 3 in Fig. 1 denotes the linear flow channel, serial number 4 in Fig. 1 denotes the flow channel of the turning transition section, serial number 5 in Fig. 1 denotes the ridge, and serial

number 6 in Fig. 1 denotes the flow channel of the discharge section. The dimensions of the novel symmetrical serpentine flow channels were 1.2 mm in width, 1.2 mm in depth and 1.2 mm landing.

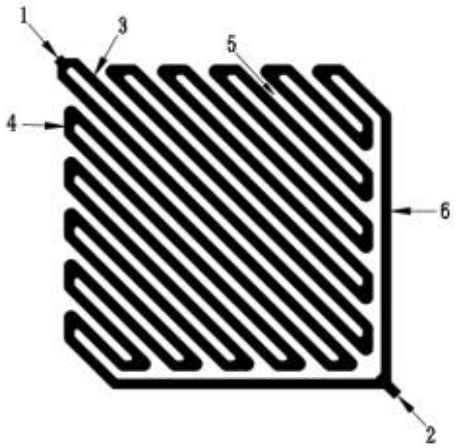

Figure 1. Geometrical schematic diagram for the new SSFF

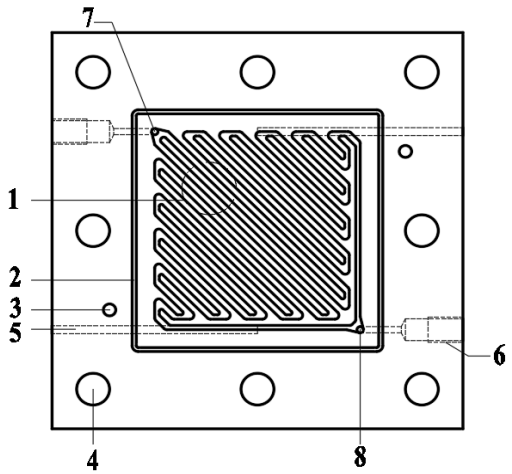

Figure 2. Schematic geometrical diagram for the new SSFF bipolar plate

The bipolar plate with the new symmetrical serpentine flow field (SSFF) was designed in this work and is presented in Fig. 2. Serial number 1 in Fig. 2 denotes the SSFF as shown in Fig.1; serial number 2 in Fig. 2 denotes the sealing groove, which is used for preventing gas leakage; serial numbers 3 and 4 in Fig. 2 represent positioning holes and bolt holes, respectively, which are used for facilitating positioning and assembly when installing the bipolar plate; serial number 5 in Fig. 2 denotes the temperature measuring hole, which is used for monitoring the temperature of the bipolar plate; serial number 6 in Fig. 2 denotes flow guide holes; serial number 7 in Fig. 2 denotes the flow field inlet, and serial number 8 in Fig. 2 denotes the outlet of flow field. The sizes for the novel SSFF bipolar plate of cathode were 100mm in length, 100mm in width and 12.5mm in thickness. The material of the bipolar plate is graphite in the work. The three dimensional geometrical model for the new SSFF bipolar plate is presented in Fig. 3.

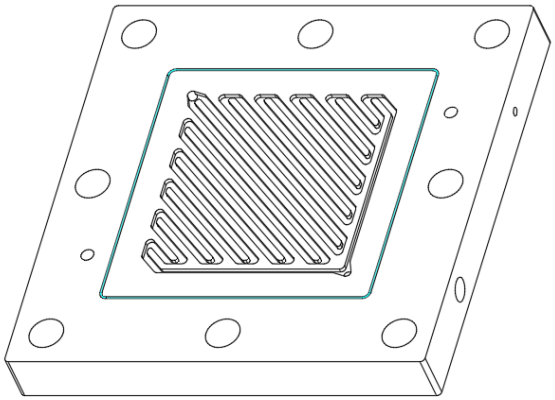

Figure 3. Three dimensional geometrical model for the new SSFF bipolar plate

3. NUMERICAL SIMULATION

3.1 Governing equations and Assumptions

For the purpose of studying the influence of the flow field structure for the bipolar plate on dynamic transmission and output performance of the PEMFC, the governing equations used in this work are as shown as follows [23-25].

The continuity equation:

$$\frac{\partial(\varepsilon\rho)}{\partial t}+\nabla\cdot\left(\varepsilon\rho\vec{u}\right)=S_m \qquad (1)$$

where S_m is the mass source term.

The mass source term, S_m, are zero for the GDLS and the flow channels, for the CLs are as follow:

Anode: $S_m=S_{H_2}=-\frac{M_{H_2}}{2F}i_a$ (2)

Cathode: $S_m=S_{O_2}+S_{H_2O}=\frac{M_{H_2O}}{2F}i_c-\frac{M_{O_2}}{4F}i_c$ (3)

Momentum conservation equation:

$$\frac{\partial\left(\varepsilon\rho\vec{u}\right)}{\partial t}+\nabla\cdot\left(\varepsilon\rho\vec{u}\vec{u}\right)=-\varepsilon\nabla P+\nabla\cdot\left(\varepsilon\mu\nabla\vec{u}\right)+S_u \qquad (4)$$

where S_u is the momentum source term.

Energy conservation equation:

$$\frac{\partial\left(\varepsilon\rho c_pT\right)}{\partial t}+\nabla\cdot\left(\varepsilon\rho c_p\vec{u}T\right)=\nabla\cdot\left(k_{eff}\nabla T\right)+S_T \qquad (5)$$

where S_T is the energy source term.

Species transport equation:

$$\frac{\partial(\varepsilon c_k)}{\partial t}+\nabla\cdot\left(\varepsilon\vec{u}c_k\right)=\nabla\cdot\left(D_k^{eff}\nabla c_k\right)+S_k \qquad (6)$$

where S_k is the species source term.

The mass source term, S_k, are zero for the GDLs and the flow channels, for the CLs are as follows:

$$S_{\mathrm{H_2}}=-\frac{1}{2\mathrm{F}}i_a \qquad (7)$$

$$S_{\mathrm{O_2}}=-\frac{1}{4\mathrm{F}}i_c \qquad (8)$$

$$S_{\mathrm{H_2O}}=\frac{1}{2\mathrm{F}}i_c \qquad (9)$$

Bulter-Volmer equation:

$$S_a=j_a^{ref}\left(\frac{c_{\mathrm{H_2}}}{c_{\mathrm{H_2},ref}}\right)^{\gamma_a}\left(e^{\alpha_a\mathrm{F}\eta_a/RT}-e^{-\alpha_c\mathrm{F}\eta_a/RT}\right) \qquad (10)$$

$$S_c=j_c^{ref}\left(\frac{c_{\mathrm{O_2}}}{c_{\mathrm{O_2},ref}}\right)^{\gamma_c}\left(e^{-\alpha_c\mathrm{F}\eta_c/RT}-e^{\alpha_a\mathrm{F}\eta_c/RT}\right) \qquad (11)$$

Current conservation equation:

$$\nabla\cdot\left(\sigma_{\mathrm{sol}}\nabla\phi_{\mathrm{sol}}\right)+S_{\mathrm{sol}}=0 \qquad (12)$$

$$\nabla\cdot\left(\sigma_{\mathrm{mem}}\nabla\phi_{\mathrm{mem}}\right)+S_{\mathrm{mem}}=0 \qquad (13)$$

where σ_{sol} is the electrical conductivity of the solid zone, σ_{mem} is the membrane electrical conductivity.

In this work, following assumptions were used for the numerical simulation [26-28]: (1) the modeled PEMFC flowing system is essentially laminar; (2) the reactant gases are considered to be incompressible ideal gases; (3) gravitational effects are ignored; (4) the temperature distribution in the PEMFC is uniform; (5) only the gas phase contain water; (6) reactant gases cannot permeate through the electrolyte; (7) electrons and protons can only transport through the solid phase and the electrolyte, respectively; (8) on the anode side of the PEMFC, two different species are taken into consideration: hydrogen and water. On the cathode side, three different species are taken into consideration: oxygen, water, and nitrogen; (9) the PEMFC operates at the steady state.

3.2 The models for the numerical simulation

Two three-dimensional solid models for the PEMFC were established in this work and are exhibited in Fig. 4 and Fig. 5, correspondingly. The first model was for the PEMFC which consisted of the anode and cathode bipolar plates with the CSFF, PEM, GDLs and CLs. The second model was for the PEMFC, including the anode bipolar plate with the CSFF and the cathode bipolar plate with the SSFF, PEM, GDLs and CLs. The second model was the same as the first model except for the cathode flow field, i.e. the cathode bipolar plate with the CSFF was for the first model, while the cathode bipolar

plate with the SSFF was for the second model. The dimensions of the two models are presented in Table 1.

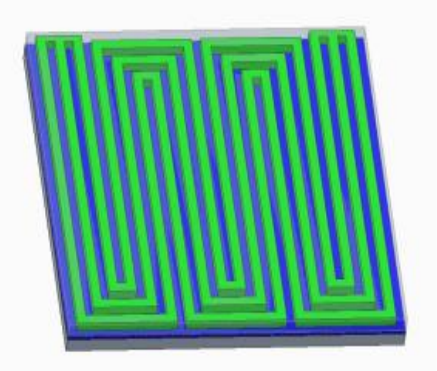

Figure 4. The first three-dimensional solid model for the PEMFC

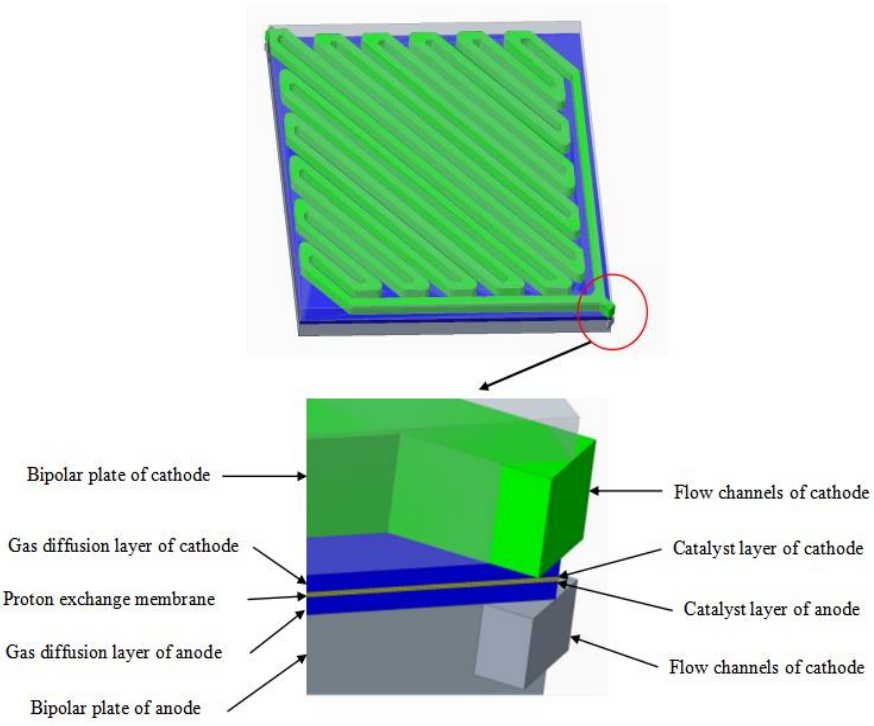

Figure 5. The second three-dimensional solid model for the PEMFC

Based on Computational Fluid Dynamic(CFD) method and the two solid models mentioned above, two three-dimensional CFD models of the PEMFC were established for the simulation using ANSYS 18.0. The three-dimensional CFD model from the first solid model of the PEMFC consisted of 4008720 elements and is shown in Fig. 6. The three-dimensional CFD model from the second solid model of the PEMFC consisted of 4086236 elements and is shown in Fig. 7. Both two CFD models chose the hexahedral element type when they were meshed. Considering the effect of mesh density on simulation accuracy and computation time for the simulation, various components employed varied

element sizes. The element size for bipolar plates of anode and cathode were set as 0.3mm. The element sizes for catalyst layers and proton exchange membrane were set as 0.005mm and 0.01mm, correspondingly. The Table 2 shows the current densities at 0.5V from various simulations for the PEMFC with the CSFF bipolar plate in the cathode. The Table 3 shows the current densities at 0.5V from various simulations for the PEMFC with the SSFF bipolar plate in the cathode. It is evident from Table 2 and Table 3 that the results are sufficiently accurate according to mesh size with 4008720 elements for the PEMFC with the CSFF bipolar plate and 4086236 elements for the PEMFC with the SSFF bipolar plate, respectively.

Table 1. Dimensions of the two models

Parameter	Value
Anode channel depth	0.6[mm]
Cathode channel depth	1.2[mm]
Anode and cathode channel width	1.2[mm]
Anode and cathode rib width	1.2[mm]
Cell active area	2500[mm^2]
GDL thickness	0.255[mm]
BPP thickness	12.5[mm]
CL thickness	0.016[mm]
Membrane thickness	0.025[mm]

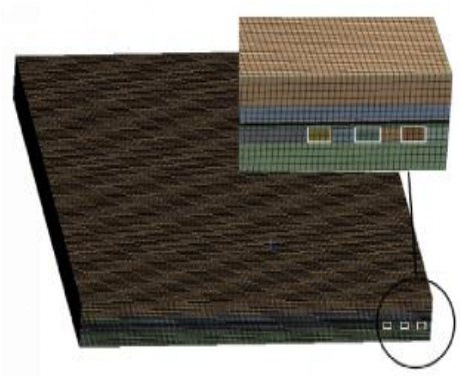

Figure 6. The first CFD model for simulation

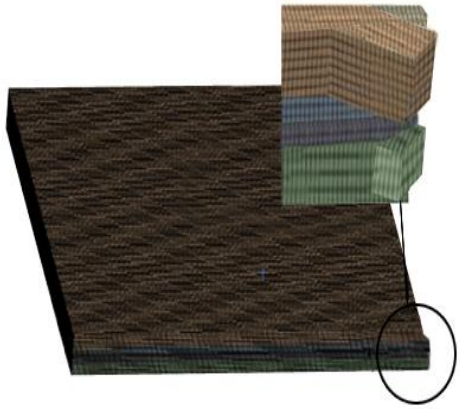

Figure 7. The second CFD model for simulation

Table 2. The current densities at 0.5V from various simulations for the PEMFC with CSFF bipolar plate in the cathode

Mesh size (number of elements)	Current density (A·cm-2)
1246895	968
4008720	1106
7927684	1110

Table 3. The current densities at 0.5V from various simulations for the PEMFC with the SSFF bipolar plate in the cathode

Mesh size (number of elements)	Current density (A·cm-2)
2058691	1055
4086236	1202
8042678	1208

3.3 Boundary conditions

The boundary conditions for the PEMFC were specified with mass flow inlet and pressure outlet, respectively. The pressure and temperature for the PEMFC were set as 1 atm and 353K. The anode mass flow and cathode mass flow were 3.9×10^{-7}kg/s and 1.8×10^{-5} kg/s, depending on stoichiometry 1.5 and stoichiometry 2.0, respectively. Physical properties and electrochemical parameters are listed in Table 4.

Table 4. Physical and electrochemical parameters

Parameter	Value
Anode and cathode pressure (atm)	1
Cell temperature (K)	353
H_2 and Air relative humidity (%)	100
Anode exchange current density (A/m^3)	2×10^9
Cathode exchange current density at the (A/m^3)	1×10^5
Anode exchange coefficient	0.5
Cathode exchange coefficient	1
Anode concentration exponent	0.5
Cathode concentration exponent	1.0
H_2 reference diffusivity (m^2/s)	1.10×10^{-4}
O_2 reference diffusivity (m^2/s)	3.23×10^{-5}
H_2O reference diffusivity (m^2/s)	7.35×10^{-5}
GDL porosity	0.78
CL porosity	0.5
Membrane equivalent weight (kg/kmol)	1100

3.4. Results and discussion

3.4.1 Distribution of oxygen mass fraction

The distribution of oxygen mass fraction at the cathode CL-GDL interface for the PEMFC with two different flow field bipolar plates at 0.5V voltage is shown in Fig. 8. The distribution of oxygen mass fraction at the cathode CL-GDL interface for the PEMFC with the CSFF bipolar plate is showed in Fig. 8(a). The distribution of oxygen mass fraction at the cathode CL-GDL interface for the PEMFC with the SSFF bipolar plate is presented in Fig. 8(b). From Fig. 8, it is evident that distribution of oxygen mass fraction at the cathode CL-GDL interface corresponding to the bipolar plate ridges and channels for the PEMFC with the SSFF bipolar plate were relatively uniform than that of the PEMFC with the CSFF bipolar plate. For two different flow fields, the oxygen mass fraction at the cathode CL-GDL interface corresponding to the bipolar plate channels was greater than the oxygen mass fraction at the cathode CL-GDL interface corresponding to the bipolar plate ridges, and the oxygen mass fraction had a decreasing trend from inlet to outlet along the flow channels. Besides, for the PEMFC with the CSFF bipolar plate, the maximum value and minimum value of oxygen mass fraction were 0.187 and 0.089, and the average mass fraction of oxygen at the cathode CL-GDL interface was 0.15. For the PEMFC with the SSFF bipolar plate, the maximum value and minimum value of oxygen mass fraction were 0.194 and 0.162, and the average mass fraction of oxygen at the cathode CL-GDL interface was 0.184, which was higher than that of the PEMFC with the CSFF bipolar plate at the same conditions. The simulated results exhibit that the flow field structure (SSFF) of the cathode bipolar plate for the PEMFC had an important effect on the oxygen transportation at the cathode CL-GDL interface. The PEMFC with the SSFF had a relatively uniform oxygen distribution and greater average mass fraction of oxygen at the cathode CL-GDL interface. The reasons are that the design of the SSFF not only reduces the gas loss along the flow channel during the transmission process, but also enhances the transmission of the

reaction gas between the flow channels. In [15], it can be concluded that the stepped flow field had a great advantage in the uniformity of gas distribution compared with traditional parallel flow field. The model predictions show that the ZPFF flow field designs provide more uniform distributions of oxygen in [20]. And The baffle plate installed in the PEMFC flow channel increases the local gas velocity, which can promote the reactant gas transport in [22].

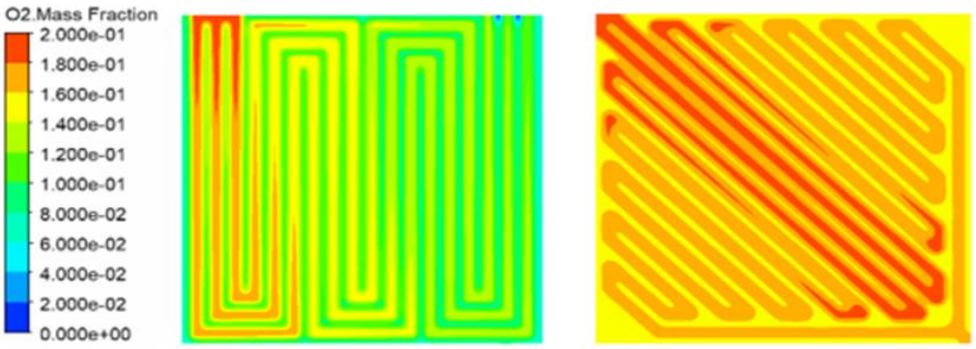

Figure 8. Distribution of oxygen fraction at the cathode CL-GDL interface for the PEMFC with (a) the CSFF, and with (b) the SSFF

In order to further study the distribution of oxygen mass fraction at the cathode CL-GDL interface for the PEMFC with two different flow field bipolar plates at 0.5V voltage, a path was defined along the direction from the inlet to the outlet corresponding to the flow channels. Fig. 9 shows the start point and direction of the path for two different flow field bipolar plates. Fig. 9(a) presents the start point (point A) and direction of the path (from point A to point B) for CSFF bipolar plate. Fig. 9(b) presents the start point (point C) and direction of the path (from point C to point D) for SSFF bipolar plate. Fig. 10 presents variation of the oxygen mass fraction distribution along the path at the CL-GDL interface for the PEMFC with two different flow field bipolar plates. For CSFF bipolar plate, the oxygen mass fraction had the decreasing trend along the path from point A to point B. While for SSFF bipolar plate, the oxygen mass fraction had a relatively stable trend along the path from point C to point D, and the value of oxygen mass fraction was almost greater than that of CSFF bipolar plate. The results indicate the superiority of SSFF bipolar plate on enhancing oxygen transport. The model reveals that WSFF was overall better than CSFF in promoting oxygen transport though the diffusion layer in [29]. And the results reveal that 3D wave flow channel was overall better than straight channel in promoting reactant gases transport in [30].

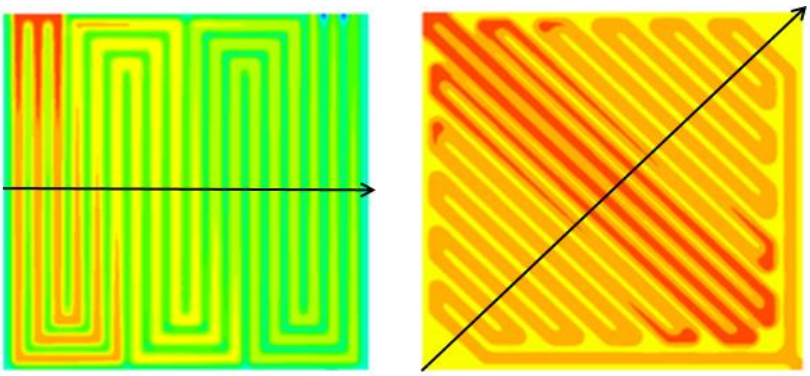

(a) (b)

Figure 9. The start point and direction of the path for (a) CSFF bipolar plate, and for (b) CSFF bipolar plate

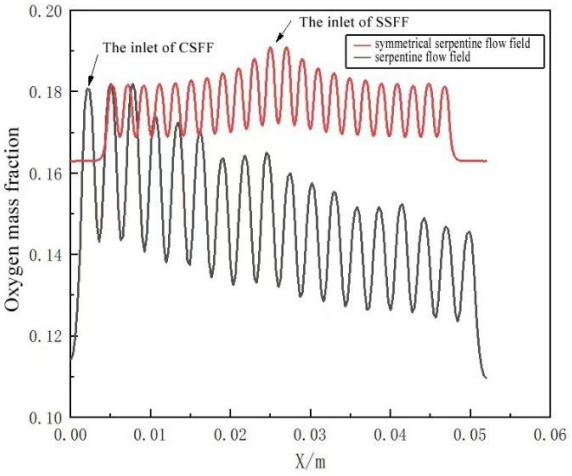

Figure 10 Variation of the oxygen mass fraction distribution along the path at the CL-GDL interface for the PEMFC with two different flow field bipolar plates

3.4.2 Distribution of water mass fraction

The distribution of water mass fraction at the cathode CL-GDL interface for PEMFC with two different flow field bipolar plates at 0.5V voltage is shown in Fig. 11. The distribution of water mass fraction at the cathode CL-GDL interface for PEMFC with the CSFF bipolar plate is presented in Fig. 11(a). The distribution of water mass fraction at the cathode CL-GDL interface for PEMFC with the SSFF bipolar plate is presented in Fig. 11(b). From Fig. 11, it is clearly that the distribution of water mass fraction at the cathode CL-GDL interface corresponding to the bipolar plate ridges and channels for the PEMFC with the SSFF bipolar plate were relatively uniform than that of the PEMFC with the CSFF bipolar plate. For two different flow field, the water mass fraction at the cathode CL-GDL interface corresponding to the bipolar plate ridges was greater than the water mass fraction at the cathode CL-GDL interface corresponding to the bipolar plate channels, and the water mass fraction had an increasing trend from inlet to outlet along the flow channels. Besides, for the PEMFC with the CSFF bipolar plate, the maximum value and the minimum value of water mass fraction were 0.1374 and 0.111, and the average mass fraction of water at the cathode CL-GDL interface was 0.123. For the PEMFC

with the SSFF bipolar plate, the maximum value and minimum value of water mass fraction were 0.1237 and 0.1107, and the average mass fraction of water at the cathode CL-GDL interface was 0.117, which was less than that of the PEMFC with the CSFF bipolar plate at the same conditions. The simulated results indicate that the flow field structure (SSFF) of the cathode bipolar for the PEMFC had an important effect on the water removal at the cathode CL-GDL interface. The PEMFC with the SSFF had a relatively uniform water distribution and lower average mass fraction of oxygen at the cathode CL-GDL interface. The reasons are that the design of the SSFF not only enhances the performance of gas transport between the channels, but also improves the forced convection of the gas to the ridge, which means the product water is more easily be removed from the flow channels. In [15], the novel stepped field design is beneficial to the water drainage and alleviate the flooding phenomenon at cathode and serious flooding in the parallel flow field of traditional PEMFC. And the model predictions show that the ZPFF flow field design provide more uniform water content in [20].

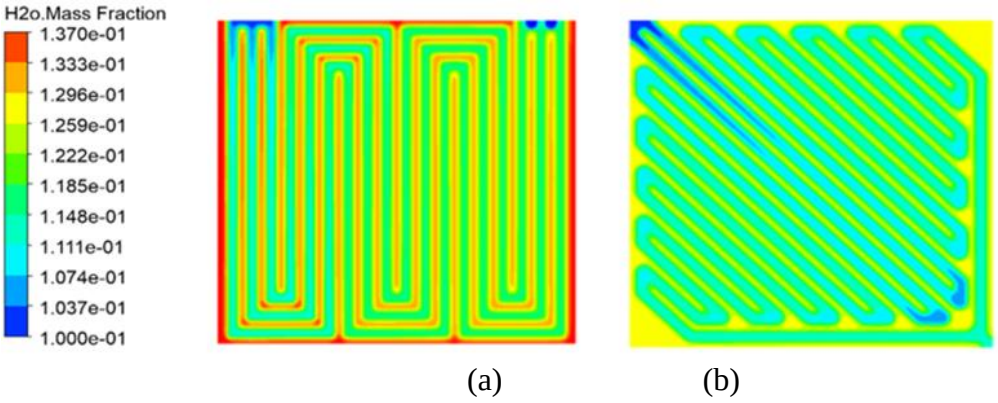

Figure 11. Distribution of water mass fraction at the cathode CL-GDL interface for the PEMFC with (a) the CSFF bipolar plate, and with (b)the SSFF bipolar plate

In order to further study the distribution of water mass fraction at the cathode CL-GDL interface for the PEMFC with two different flow field bipolar plates at 0.5V voltage, a path was defined along the direction from the inlet to the outlet corresponding to the flow channels. Fig. 12 shows the start point and direction of the path for two different flow field bipolar plates. Fig. 12(a) presents the start point (point A) and direction of the path (from point A to point B) for CSFF bipolar plate. Fig. 12(b) presents the start point (point C) and direction of the path (from point C to point D) for SSFF bipolar plate. Fig. 13 exhibits variation of the water mass fraction distribution along the path at the CL-GDL interface for the PEMFC with two different flow field bipolar plates. For CSFF bipolar plate, the water mass fraction had the increasing trend along the path from point A to point B. While for SSFF bipolar plate, the oxygen mass fraction had a relatively stable trend along the path from point C to point D, and the value of oxygen mass fraction was almost less than that of CSFF bipolar plate. The results proved the superiority of SSFF bipolar plate on enhancing water remove. So the design of SSFF bipolar plate could effectively prevent water flooding in the PEMFC. In [29], the model reveals that WSFF is overall better than CSFF

in removing liquid water accumulated in microstructure. And the similar result of 3D wave flow field also occurred in [30].

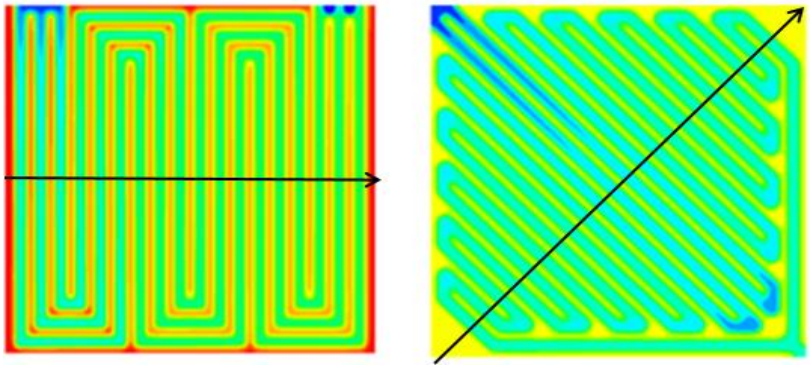

(a) (b)

Figure 12. The start point and direction of the path for (a) CSFF bipolar plate, and for (b) CSFF bipolar plate

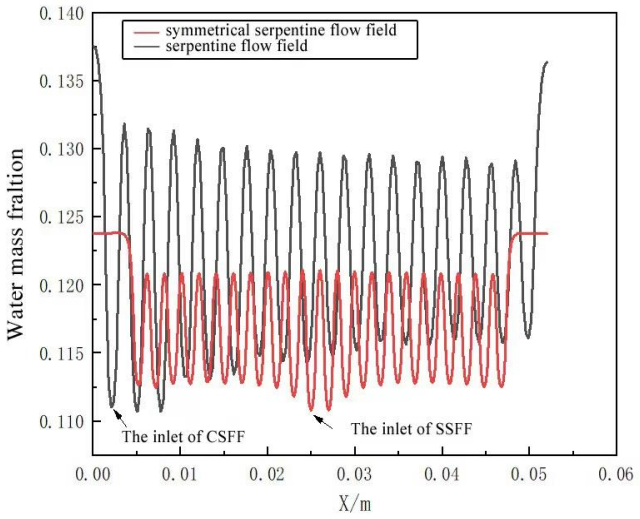

Figure 13. Variation of the water mass fraction distribution along the path at the CL-GDL interface for the PEMFC with two different flow field bipolar plates

3.4.3 Output performance

Fig. 14 presents the simulation results of the electrochemical performance for the PEMFC with two different flow field bipolar plates. Fig. 14(a) shows the polarization curves (voltage versus current density curve) for the PEMFC with the SSFF bipolar plate and the CSFF bipolar plate. Fig. 14(b) presents the power density curves (power density versus current density curve) for the PEMFC with the SSFF bipolar plate and the CSFF bipolar plate. From Fig. 14 (a), it can be seen that the electrochemical

performance of the PEMFC with the SSFF bipolar plate had no obvious change compared with the electrochemical performance of the PEMFC with the CSFF bipolar plate when the current density was less than 300mA/cm2. When the current density exceeded 300mA/cm2, the flow field structure started to have an important effect on electrochemical performance of the PEMFC. At voltage of 0.5V, the current density of the PEMFC with the CSFF bipolar plate was 944 mA/cm2. While the current density of the PEMFC with the SSFF bipolar plate was 1202 mA/cm2 at voltage of 0.5V, which was increased by 258 mA/cm2 in the identical conditions. From Fig. 10(b), it can be seen that the maximum power density for the PEMFC with the CSFF bipolar plate was 0.489 W/cm2, while the maximum power density for the PEMFC with the SSFF bipolar plate was 0.601 W/cm2. The maximum power density for the PEMFC was enhanced by 22.9% by adopting the SSFF. It exhibits that the PEMFC with the SSFF bipolar plate had better electrochemical performance due to the use of SSFF. The reasons is that the PEMFC with the new SSFF bipolar plate had better oxygen transportation (see Fig. 8) and better water removal(see Fig. 11) than the PEMFC with the CSFF bipolar plate. In [15], compared with fuel cell with parallel flow field, the net power of fuel cell with stepped flow field was increased by 21.5%. It is found that the maximum power output of the CBFF was increased by 8.475% than the serpentine flow field's in [18]. In [29], there is a 17.8% increment in the peak power density due to the use of WSFF.

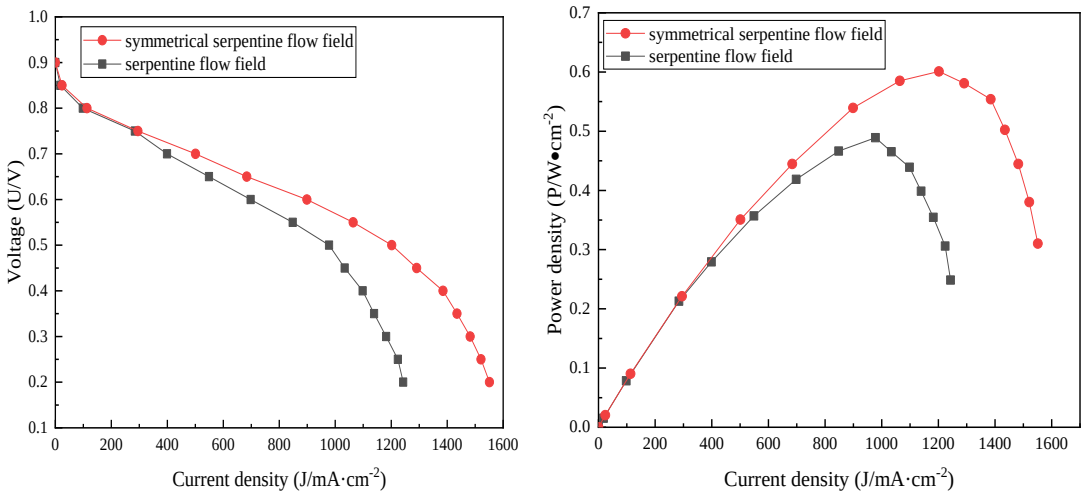

Figure 14. The simulation results of (a) polarization curves and (b) power density curves for the PEMFC with two different flow field bipolar plates

4. EXPERIMENT

4.1 PEMFC preparation

In this work, the experimental study was conducted using the Arbin PEMFC Instrument. The single PEMFC used for experiment consisted of elastomeric gaskets, graphite bipolar plates, current collectors, metal endplates with the Nylon layers, MEA, and bolts. The MEA includes a PEM, CLs and GDLs. Toray carbon paper (TGP-H-60) was utilized to make the GDL for the MEA in this experiment.

The PEM was constructed using Nafion 211 membrane, and thickness of the membrane was 25μm. The CL contained 0.48 mg/cm2 Pt/C(60%) loading on both anode side and cathode side, and the CL had an 25 cm^2 active area. The thickness of CL was 16μm. The MEA was placed between anode bipolar plate and cathode bipolar plate. The anode bipolar plate presented in Fig. 15 were with the conventional serpentine flow channels with 1.2mm in width, 0.6 mm in channel depth and 1.2mm landing. The cathode bipolar plate shown in Fig. 16 was with the new symmetrical serpentine flow channels with 1.2mm in width, 1.2 mm in depth and 1.2mm landing. The experimental PEMFC has the same shape and dimensions as the simulated PEMF with the new symmetrical serpentine flow channels mentioned above.

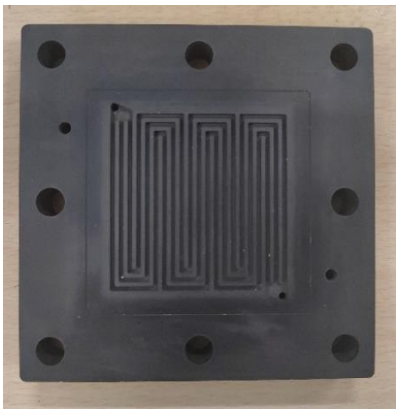

Figure 15. The picture of the anode bipolar plate with the conventional serpentine flow channels

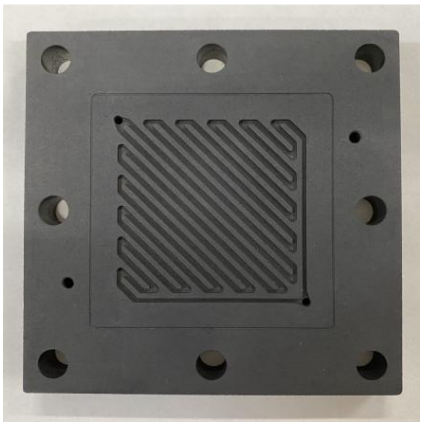

Figure 16. The picture of the cathode bipolar plate with the new symmetrical serpentine flow channels

4.2. PEMFC testing system

For investigating experimentally the electrochemical performance for the PEMFC with the novel SSFF and to verify accuracy and feasibility of the numerical simulation, the electrochemical performance tests were conducted using the Arbin PEMFC Instrument. The schematic diagram of the PEMFC test system is presented in Fig.17.

Before hydrogen fuel entered the anode on one side of the fuel cell and oxygen from the air was sent to the cathode on the other side, the hydrogen and oxygen/air were humidified. The testing system includes a check value to prevent backflow, a upstream pressure gauge and mass flux controllers to monitor gas pressure of the inlet and the fluxes of hydrogen and air, respectively. And thermocouples were installed in the anode bipolar plate and cathode bipolar plate for controlling temperature.

After the background values were attained, hydrogen and air entered the PEMFC from the anode and cathode through the dew point humidifier of anode and cathode. In the process of testing, the operating temperature for the PEMFC was maintained at 353K, the hydrogen flow rate was 285 ml/min, the air flow rate was 905 ml/min, the relative humidity of both the hydrogen and air was maintained at 100%, and gas back pressure (gauge pressure) for the fuel cell was 0 MPa.

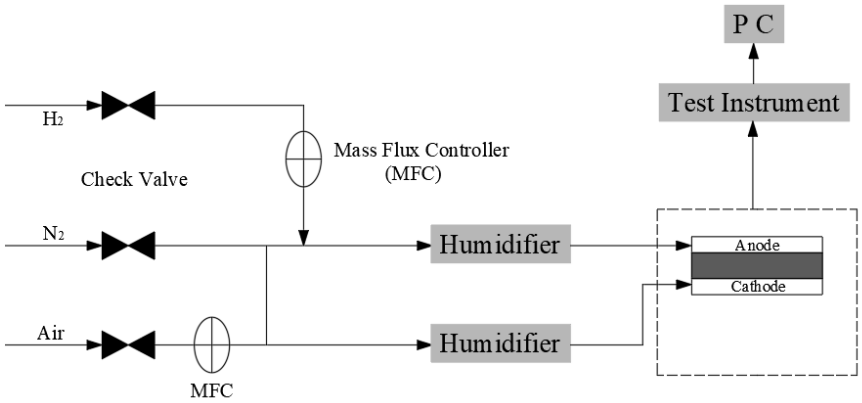

Figure 17. The schematic diagram of the PEMFC test system

4.3. Experiment results and discussion

The electrochemical performance of the PEMFC with the SSFF bipolar plate based on test is shown in Fig.18. The test results of the polarization curve for PEMFC with the SSFF bipolar plate are presented in Fig 18(a). The test results of the power density curve for the PEMFC with the SSFF bipolar plate are exhibited in Fig. 18(b). The simulation results of polarization curve and power density curve are also shown in Fig. 18 for comparison. The test result indicates that the maximum power density of the PEMFC with the new SSFF bipolar plate was 0.583 W/cm2. As demonstrated in Fig. 18 (a) and Fig. 18 (b), the test results were matched well with the simulation results.

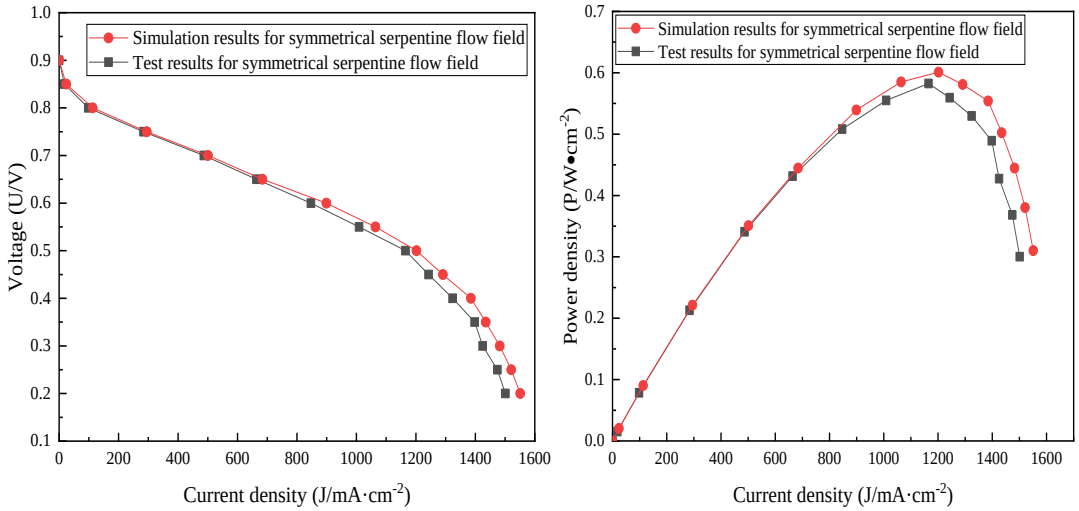

Figure 18. The test results of (a) polarization curve and (b) power density curve

5. CONCLUSIONS

In this paper, a new symmetrical serpentine flow field (SSFF) was presented. A single PEMFC with the new SSFF bipolar plate was designed and studied. And two three-dimensional CFD models for the PEMFC with the CSFF and the novel SSFF bipolar plate were established based on Computational Fluid Dynamics (CFD) method. And then, numerical simulations were conducted using the FLUENT PEM fuel cell module. In addition, the electrochemical performance test was performed for the PEMFC with the novel SSFF bipolar plate. The following conclusions can be drawn.

(1) The results of simulation present that flow field structure of the cathode bipolar plate in the PEMFC had a significant influence on the oxygen mass fraction distribution at the cathode CL-GDL interface. The cathode CL-GDL interface for the PEMFC with the new SSFF had a relatively uniform oxygen distribution and higher average mass fraction of oxygen. The simulated results also indicate that flow field fracture of the cathode bipolar plate in the PEMFC had an important effect on the water removal at the cathode CL-GDL interface. The cathode CL-GDL interface for the PEMFC with the new SSFF had a relatively uniform water distribution and lower average mass fraction of water. The above results proved the superiority of SSFF bipolar plate on enhancing oxygen transport and water remove.

(2) The results of simulation present that the flow field structure had a remarkable effect on the output performance for the PEMFC. The PEMFC with the novel SSFF bipolar plate had better electrochemical performance than the PEMFC with the CSFF bipolar plate at the same circumstances. Specially, the maximum power density for the PEMFC with the novel SSFF bipolar plate was increased by 22.9% in this work.

(3) The result of the electrochemical performance test also shows that the PEMFC with the new SSFF bipolar plate had better electrochemical performance than the PEMFC with the CSFF bipolar plate.

The results of test were matched well with the results of simulation. This work may help the component manufacturers to assess the effect of flow field design of bipolar plate on PEMFC performance.

ACKNOWLEDGEMENT
This work was sponsored by the Natural Science Foundation of China (52275152).

References

1. F.A. Kharir, M.M. Barzegari and H. Talebi-Ghadikolaee, *Int. J. Hydrogen Energy*., 46 (2021) 79.
2. M. Dadfar, M. Salehi and M.A. GOLOZAR, *Int. J. Hydrogen Energy*., 42 (2017) 41.
3. M. Sánchez-Molina, E. Amores and N. Rojas, *Int. J. Hydrogen Energy*., 46 (2021) 79.
4. W.M. Yan, C.Y. Chen and C.H. Liang, *Energy.*, 186 (2019) 115836.
5. Y. Wang, Q. Tan and B. Huang, *J. Alloys Compd*., 879 (2021) 160470.
6. C. Alegre, L. Álvarez-Manuel and R. Mustata, *Int. J. Hydrogen Energy*., 44 (2019) 25.
7. H.C. Kang, K.M. Jum and Y.J. Sohn, *Int. J. Hydrogen Energy*., 44 (2019) 43.
8. T. Wilberforce, Z. Elhassan and E. Ogungbemi, *Renewable Sustainable Energy Rev*., 111 (2019) 236.
9. D.K. Dang, B. Zhou, *Int. J. Hydrogen Energy*., 46 (2021) 40.
10. B. Randrianarizafy, P. Schott and M. Chandesris, *Int. J. Hydrogen Energy*., 43 (2018) 18.
11. Z. Wang, Y. Zeng and S. Sun, *Int. J. Hydrogen Energy*., 42 (2017) 34.
12. M.E. Youssef, R.S. Amin and K.M. El-Khatib, *Arabian J. Chem.*, 11 (2018) 5.
13. A. Mahdavi, A.A. Ranjbar and M. Gorji, *Appl. Energy*., 228 (2018) 656, 228(656-66.
14. C. Zhang, J. Ma and X. Liang, *J. Mater. Process. Technol*., 262 (2018) , 32.
15. X. Chen, Y. Chen and Q. Liu, *Energy Rep*., 7 (2021) 336.
16. F. Ramin, H. Sadeghifar and A. Torkavannejad, *Int. J. Heat Mass Transfer*., 129 (2019) 1151.
17. J. Liu, J. Tan and W. Yang, *Energy*., 229 (2021) 120796.
18. L. Xia, Z. Yu and G. Xu, *Energy Convers. Manage*., 247 (2021) 114707.
19. D.H. Chang and S.Y. Wu, *Int. J. Hydrogen Energy*., 40 (2015) 35.
20. Z. Liao, L. Wei and A.M. Dafalla, *Int. J. Heat Mass Transfer*., 181 (2021) 121900.
21. H. Huang, H. Lei and M. Liu, *Energy Convers. Manage*., 226 (2020) 113546.
22. Y. Yin, X. Wang and X. Shangguan, *Int. J. Hydrogen Energy*., 43 (2018) 16.
23. S. Liu, T. Chen and Y. Xie, *Int. J. Hydrogen Energy*., 44 (2019) 56.
24. G. Zhang, K. Jiao, *Energy Convers. Manage*., 176 (2018) 409.
25. R. Chen, Y. Qin and S. Ma, *Int. J. Hydrogen Energy*., 45 (2020) 54.
26. Z. Zhang, W. Liu and Y. Wang, *Int. J. Hydrogen Energy*., 1 (2019) 44.
27. S. Ebrahimi, S. Roshandel and K. Vijayaraghavan, *Int. J. Hydrogen Energy*., 41 (2016) 47.
28. M. Liu, H. Huang and X. Li, *Int. J. Hydrogen Energy*., 46 (2021) 75.
29. W. Li, Q. Zhang and C. Wang, *Appl. Energy*., 195 (2017) 278.
30. X. Chen, Z. Yu and C. Yang, I *Int. J. Hydrogen Energy*., 46 (2021) 19.